Dynamical reconstruction of the upper-ocean state in the Central Arctic during the winter period of the MOSAiC Expedition

Ivan Kuznetsov[a], Benjamin Rabe[a], Alexey Androsov[a], Ying-Chih Fang[b], Mario Hoppmann[a], Alejandra Quintanilla-Zurita[a], Sven Harig[a], Sandra Tippenhauer[a], Kirstin Schulz[c], Volker Mohrholz[d], Ilker Fer[e], Vera Fofonova[a], and Markus Janout[a]

[a]Alfred-Wegener-Institut Helmholtz-Zentrum für Polar- und Meeresforschung, Bremerhaven, Germany
[b]National Sun Yat-sen University University, 80424 Kaohsiung, Taiwan
[c]Oden Institute for Computational Engineering and Sciences, The University of Texas at Austin, Austin, TX, United States
[d]Leibniz-Institute for Baltic Sea Research Warnemünde, Germany
[e]Geophysical Institute, University of Bergen and Bjerknes Center for Climate Research, Bergen, Norway

Correspondence: Ivan Kuznetsov (ivan.kuznetsov@awi.de)

Abstract. This work presents a dynamical reconstruction of the ocean state, based on observations from the Multidisciplinary Observatory for the Study of Arctic Climate (MOSAiC) experiment. The data used in this study were collected between October 2019 and January 2020 in the Amundsen Basin. Analyzing observational data to assess tracer field gradients and upper ocean dynamics is highly challenging when measurement platforms drift with the ice pack, due to continuous changes in drift speed and direction. We have equipped the new version of the coastal branch of the global finite volume sea-ice ocean model (FESOM-C) with a nudging method developed specifically for MOSAiC data. Model nudging was carried out assuming a quasi-steady-state. Overall, the model can reproduce the lateral and vertical structure of the temperature, salinity, and density fields, which allows for projecting dynamically consistent features of these fields onto a regular grid. We identify two separate depth ranges of enhanced eddy kinetic energy, which are located around two maxima in buoyancy frequency: the depth of the upper halocline and the depth of the warm (modified) Atlantic Water. Simulations reveal a notable decrease in surface layer salinity and density towards the north but no significant gradients from west to east. However, we do find an increase in mixed layer depth in that direction, with a 0.084 m/km gradient at 0.6 m/km standard deviation, indicating opposite characteristics compared to the south-north direction in the Amundsen Basin. The model resolves several stationary eddies in the warm Atlantic Water and provides insights into the associated dynamics. The model output can be used for further analysis of the thermohaline structure and related dynamics associated with mesoscale and submesoscale processes in the Central Arctic, such as estimates of heat fluxes or mass transport. The developed nudging method can be utilized to incorporate observational data from a diverse set of instruments and for further analysis of data from the MOSAiC expedition.

1 Introduction

Mesoscale and submesoscale eddies have been observed in many parts of the world's oceans, including the Arctic. The fluxes driven by those eddies play a significant role in Arctic Ocean dynamics, such as the ventilation of the halocline, and the transport of organic and inorganic matter, e.g. nutrients and carbon, heat and salt (Dmitrenko et al., 2008; Meneghello et al.,

2021; Marcinko et al., 2015; Pnyushkov et al., 2018; Mahadevan, 2016; Mahadevan et al., 2010; Gula et al., 2022; Nishino et al., 2018; Watanabe, 2011). The majority of studies on under-ice eddy dynamics in the Arctic are focused on the ice edge or the shelf break zone, where the eddy activity is maximal, but little is known about eddies in the ice-covered central Arctic Ocean.

Analyzing Ice-Tethered Profiler and mooring data in the Canada Basin, Zhao et al. (2016) show that eddy activity is subject to high interannual variability. Pnyushkov et al. (2018) find, based on mooring observations, that eddies in the area of the boundary current in the eastern Eurasian Basin appear about once per month and have a significant role in the vertical transfer of heat within the Arctic Ocean interior. Such eddies may even persist for one or several months, according to a detailed three-dimensional analyses of an Arctic eddy in the Chuckchi Sea, based on data from a rapid shipboard survey Scott et al. (2019).

The intensity of mesoscale dynamics can be represented by the eddy kinetic energy (EKE). von Appen et al. (2022) find that mesoscale EKE is stronger in areas with low sea ice concentration. Using the results of high-resolution modeling and observational data, Meneghello et al. (2021) show that surface mesoscale activity is extremely low during the winter period, due to fast energy dissipation by friction between eddies and sea ice. The mesoscale activity is inevitably linked to submesoscale dynamics, such as filaments around mesoscale eddies (e.g. Della Penna and Gaube, 2019; Mahadevan, 2016). Vertical eddy diffusivity of mass and heat, and associated fluxes, as well as vertical velocity can be enhanced sigificantly by under-ice eddies (Manucharyan and Thompson, 2017); conversely, submesoscale flows can both enhance those fluxes and suppress them by restratifying the mixed layer (Mensa and Timmermans, 2017).

Despite the intensification of eddy dynamics at the basin boundaries, von Appen et al. (2022) note that in the central Eurasian Basin, EKE is significant in both the halocline and the Atlantic Water layer, according to high-resolution simulations. Meneghello et al. (2021) show that subsurface eddies can be explained by the baroclinic stratification and potential vorticity gradients commonly present in the Arctic interior and note the presence of EKE maxima in two layers of maximum density gradients in the Canada basin. An analysis of the dynamics of baroclinic vortices in stratified fluids, and the associated mass and heat transports, based on theoretical developments and numerical methods is given in Sokolovskiy and Verron (2014).

Eddy dynamics not only impact ocean physics but also biochemical and ecosystem processes in the Arctic Ocean. Llinás et al. (2009) illustrate the possible mechanism of zooplankton transport from the Chukchi Shelf into the interior Canada Basin by eddies. O'Brien et al. (2013) find a significant role of eddies on the particle flux, and Oziel et al. (2022) demonstrate in a modelling study that lateral submesoscale eddy transport is one of the dominating processes controlling the nitrate supply in the central Arctic Ocean. Omand et al. (2015) show that small-scale vorticity could be responsible for high concentrations of particulate organic carbon in deeper layers. According to their calculations, submesoscale, eddy-driven fluxes can contribute as much as half of the total springtime export of particulate organic carbon from the upper ocean to deeper layers in the subpolar region. Using coupled physical and ecosystem models,

Despite ongoing efforts to develop and improve climate models, the accurate representation of both mesoscale and submesoscale dynamics remains a challenge. Androsov et al. (2020) compared ocean models with various horizontal resolutions to observed ocean bottom pressure, and found only a modest correlation between the models and observations. They conclude

that high resolution is necessary in areas with high mesoscale eddy activity. According to Zhao et al. (2014), the radii of observed halocline mesoscale eddies are on the order of a few kilometers in the Arctic Ocean, where the first baroclinic Rossby deformation radius varies between 1 to 15 km (Nurser and Bacon, 2014). The necessity to resolve such small scales makes it challenging to explicitly model mesoscale and submesoscale features in global climate models due to the lack of horizontal resolution. Recent developments in ocean and coupled climate models, software, and hardware give a possibility for simulations with a very high horizontal resolution, for example Wang et al. (2020); Maslowski et al. (2008); Regan et al. (2020); Lyu et al. (2022); Hordoir et al. (2022).

Most studies on eddy dynamics in the Arctic have focused on the marginal ice zone or coastal currents, the main limitation of mesoscale and submesoscale research in the central Arctic being observational data. Unfortunately, standard methods for observing eddies, such as satellite remote sensing or glider and transect campaigns, have so far been challenging in near-perennially ice-covered seas. To fill this gap the Multidisciplinary Observatory for the Study of Arctic Climate (MOSAiC, e.g. Rabe et al., 2022) designed a Distributed Network (DN; Rabe et al., 2023) of autonomous ice-tethered systems (hereafter referred to as "buoys") around the MOSAiC Central Observatory (CO). The CO included a series of buoys, and mostly manual ocean observations at the R/V *Polarstern* and a site about 300 m away from the ship ("Ocean City"; OC). This setup enabled us to obtain regular, non-autonomous measurements during the MOSAiC expedition. The large number of extremely diverse observations, from point measurements to profiles, differ significantly both in temporal frequency, from irregular weekly measurements to measurements every 2 minutes, and in spatial resolution, from tens of kilometers to tens of meters. Moreover, the looping of the DN drift trajectory and the intersection of the trajectories of different buoys add complexity to the observed data. Nevertheless, using relatively simple data analysis methods, several mesoscale eddies have been identified in the Amundsen Basin (Hoppmann et al., 2022; Fang et al., 2023; Quintanilla-Zurita and et al., (in prep.). However, these methods have limitations in showing the overall three-dimensional picture due to the above mentioned complex drift trajectories, and analyzing the buoy measurements spatially can be challenging; in particular, estimating lateral gradients of tracers or velocity shear. This poses the question how to best analyze such scattered data and dynamics, and their role in vertical transport. One possible approach is to use interpolation techniques, such as optimal interpolation (Bretherton et al., 1976) or Data Interpolation Variational Analysis (Troupin et al., 2012; Barth et al., 2014). However, the lateral scales of phenomena on interpolated maps can be limited by distances between the observing buoy systems or parameters of the interpolation algorithm, rather than physical processes.

Reconstructing temperature, salinity, and density fields with a model by data assimilation allows estimating dynamically consistent lateral features of these fields on a regular grid. Androsov et al. (2005) and Rubino et al. (2007) used in situ observations together with three-dimensional non-hydrostatic modelling to investigate the non-stationarity of the dynamics and evolution of mesoscale chimneys in the Greenland Sea. Together with an analytical solution this allowed the authors to investigate inertial pulsations, shape, and velocity structure of these eddies, and their significant effect on open-ocean deep-penetrating convection. Assimilating high-frequency variability data, however, presents its own significant challenges: First, the assimilation time (usually once every 10 days or even daily averaging in extreme cases) significantly increases computation time. Second, the assimilation process involves averaging over a significant data radius, resulting in a smoothing effect on the assimilated data

(Androsov et al., 2018). The nature of the data has to be considered when employing advanced methods such as the four-dimensional variational method (Courtier et al., 1994; Mogensen et al., 2009) or the Parallel Data Assimilation Framework (Nerger et al., 2020). Unfortunately, the high-frequency variability and the scales of the observations inherent in the MOSAiC data make it impractical to apply these methods to eddy analysis. Alternatively, nudging has several advantages for ocean data assimilation, including its ease of implementation in complex numerical models, its low computational demands, and the smoothness of the solution over time (Ruggiero et al., 2015).

The aim of our study is to extend current knowledge of eddy dynamics in the central Arctic by using the three-dimensional regional model FESOM-C with very high vertical (up to 1 m) and horizontal (up to 250 m) resolution. We utilize observed temperature and salinity data from the MOSAiC DN buoys as part of the forcing for the numerical model, employing a nudging method with a quasi-steady-state approximation. Our objective is to present a newly developed modelling tool to reconstruct gridded fields of water properties based on MOSAiC DN observational temperature and salinity. Additionally, we aim to estimate the properties of mesosale and submesoscale dynamics and their potential variability during the MOSAiC expedition.

This paper is organized as follows. Section 2 presents the numerical model, observations, new nudging methodology, and experimental design. In section 3, we present the results of the simulations and model validation. The analysis of (sub)mesoscale dynamics and distribution of eddy kinetic energy from the reconstructed dynamical fields are discussed in Section 4. In section 5 we summarize the results.

2 Methods

2.1 FESOM-C model

The FESOM-C model used in this work (Danilov and Androsov, 2015; Androsov et al., 2019) is a coastal branch of the global Finite volumE sea ice–Ocean Model (FESOM2) (Danilov et al., 2017). In addition to the partially common interface of the models, FESOM-C has specific features that are important for our work. The model was originally developed for applications with a high horizontal resolution as fine as several meters (Neder et al., 2022; Kuznetsov et al., 2020; Fofonova et al., 2019). This model uses the discretization of cells and vertices of a finite volume, which allows the use of unstructured computational grids. We use this function to move the boundary of the computational domain away from the region of interest, the "core" of the model grid, without creating a system of nested grids. At the same time, the horizontal resolution outside the core is quite coarse, which allows us to reduce the influence of the boundary on our solution inside the core. The most important distinguishing feature from the global FESOM2 model is the possibility of using hybrid grids consisting of triangles and squares. The effectiveness of this approach to enhance stability and using larger time steps is shown by Danilov and Androsov (2015) and Androsov et al. (2019). Additionally, this branch of the model uses sigma layers in the vertical direction.

The parallel Algebraic Recursive Multilevel Solver (pARMS, (Li et al., 2003b)) used in FESOM2 was used to calculate the sea level using a semi-implicit method. Since we study the processes in the deep-water region, where the effect of bottom friction is minimal and the barotropic mode does not play a key role, we modified the scheme to a semi-implicit calculation of the sea level, omitting the solution of the block of average equations.

The thermodynamics of the sea ice model component has not been used in the current work. Alteration of the ocean surface temperature and salinity due to ice formation and melting has been implemented through model nudging towards observational data. The effect of sea ice presence on the dynamics of the ocean surface layer has been parameterized by the friction between ice and ocean. Thus, we do not take into account the additional transfer of momentum due to ice drift. The effect of ice drift has been accounted for in the turbulence closure and is described in the following section.

In contrast to previous publications, we have implemented parallel calculations based on the Message Passing Interface (MPI). For the dynamic part of the model, the MPI scheme is similar to that of FESOM2 but applied to hybrid grids. The organization of parallel output and input for boundary conditions at open surface boundaries, in contrast to the global model, were written using the PnetCDF library (Li et al., 2003a). This made it possible to take advantage of the flexibility of the previous openMP FESOM-C I/O version.

2.2 Turbulence closure

The turbulence closure equation based on the Prandtl-Kolmogorov hypothesis described in Androsov et al. (2019) is used to calculate turbulent vertical flows. Compared to the original version of the FESOM-C model, the modification of this equation concerned only the parametrization of the turbulence scale l. The need for this change is associated primarily with the parametrization of the ice-water layer and a more dynamic description of the moving Mixed Layer (ML). At the preliminary stage, an average upper bound ice-drift velocity is estimated at 0.7 m/s, which is used as an upper boundary condition for the dynamic wind speed in the turbulent energy budget equation. This parameter is used across the entire domain and throughout the entire period of the model's nudging. Since we use a quasi-steady-state approximation (see nudging section 2.5), this parameter remains unchanged throughout the entire computation process. In the second stage, the thickness of the ML h_{ml} is estimated as the depth with a practical salinity increase of 0.5 from the surface value, but minimum 20 m. This is one of the commonly used definitions of the ML depth. The exact definition of ML depth does not play a crucial role in our task. Then, the scale of turbulence in the upper ML is determined by

$$l = \frac{\kappa}{h_{ml}} \cdot Z_H \cdot Z_\zeta, \tag{1}$$

where z is the depth, positive downwards, $Z_H = z + h_{ml}$, $Z_\zeta = z + z_\zeta$, $\kappa \sim 0.4$ is the von Kármán constant and z_ζ is the roughness parameter for the ice-water layer. Underneath the surface ML h_{ml}, the scale of turbulence is given by:

$$l = \frac{\kappa}{H - h_{ml}} \cdot Z_H \cdot Z_{ml} \cdot C, \tag{2}$$

where $H = h + \zeta$ is the full water depth, $Z_{ml} = -z + (H - h_{ml}) + z_b$, z_b is the roughness parameter for the bottom and the constant $C \sim 0.01$ is set to reduce the scale of turbulence underneath the ML. This approach to determine the scale of turbulence ensures the smoothness and minimization of turbulent exchange at the boundary of the ML and the water column underneath the ML.

2.3 Model domain

The model domain is a parallelepiped in Cartesian coordinates with a solid boundary. Since the FESOM-C model allows computing on mixed unstructured meshes, we can adjust the spatial resolution without using nested grids. For the final computations, two spatial configurations of the model are used. The general conditions for these configurations were that, near the horizontal boundaries of the domain, the spatial resolution was relatively coarse, about 5 km. Such a coarse resolution at the boundaries serves two purposes: First, absorption due to the more strong dissipation of the uncertainty of the boundary information and its leveling to calculations in the core of the model is the most important in our application. Second, there are significant savings in computational resources. The first configuration of the model has a resolution of up to 1 km in the area of interest and contains 96000 nodes. This setup is mainly used at the initial modeling stage to form the initial conditions for a spatially detailed configuration of the study domain. The second configuration has a resolution of up to 250 m at the model's core and contains about 1.3 million nodes (see Figure 1). This setup is used for the final computations and data analysis. The vertical structure is the same for both configurations and contains 240 vertical σ-layers. At the same time, the upper layer up to 150 m has an effective resolution of up to one meter, which makes it possible to significantly improve the representation of the vertical aspects of the submesoscale dynamics of surface ML compared to global models. The model domain is about 660 by 525 km and limited geographically to between 90° East and 140° East longitude as well as 83° North and 87.7° North latitude.

2.4 Observational data

Here we use an observational data set obtained as part of the physical oceanography work program during the field phase of the Multidisciplinary Observatory for the Study of Arctic Climate (MOSAiC) in 2019/20 (Shupe et al., 2020). A description of the physical oceanography part of the experiment with a general description of the instruments and methodology is presented in Rabe et al. (2022). Temperature and salinity observations used in this work were obtained by various instruments: Most of the data was measured by autonomous ice-tethered systems ("buoys") within the DN originally deployed by the icebreaker *Akademik Fedorov* (Krumpen and Sokolov, 2020) radially around the icebreaker *Polarstern* tethered to the sea ice at the Central Observatory. Eight buoys termed "Salinity-Ice-Tether" (SIT) measured temperature, conductivity, and pressure, with derived salinity and depth, at five depths of 10, 20, 50, 75, and 100 m with a sampling interval of 2 to 10 minutes, with a distance between subsequent data points as small as 80 m. The sensors used on these buoys have an initial accuracy of $\pm$0.003 mS cm^{-1} for conductivity, $\pm$0.002 °C for temperature, and $\pm$0.1% of the full range for pressure. The sensor stability rating is 0.003 mS cm^{-1} and 0.0002 per month for conductivity and temperature, respectively, with a yearly rating of 0.05% of the full scale for pressure. The detailed description of the instruments and the data obtained are given by Hoppmann et al. (2022). We further, used data from three Ice-tethered profilers (ITP; Toole and Krishfield, 2016). The time between subsequent profiles varied from several hours to days, depending on the specific system. The maximum depth reached by these profilers was about 700 m. Thus, the measurements with profilers cover depths in the warm waters of Atlantic origin (referred to as "warm Atlantic Water") and beyond. A total of 1114 profiles was used for model nudging. The nudging process included additional profiles from CTD/rosette casts at the Central Observatory, both from *Polarstern* (PS-CTD; 25 profiles with depths up to 4450 m)

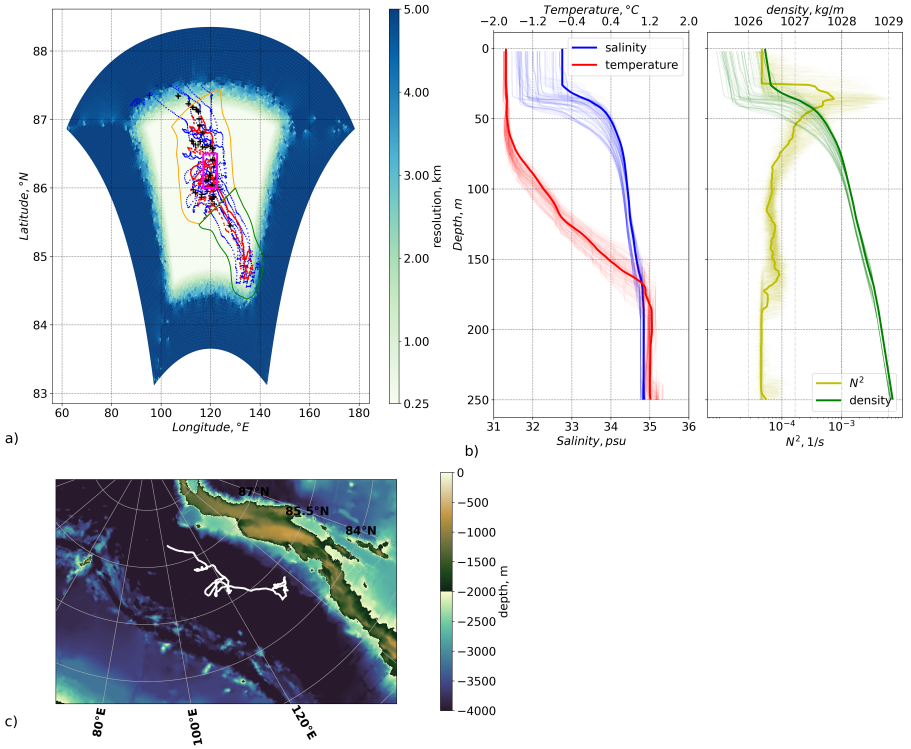

Figure 1. a) - Model domain resolution with the position of the observational data used in this study, covering a time period of ≈2.5 months. The positions of the observational data used for nudging are separated by instrument type: blue - 5 SIT buoys, with CTDs at 10,20,50,75,100 m depth (Hoppmann et al., 2022). red – PS- and OC-CTD casts (Tippenhauer et al., 2023a, b), and ITP profiles (Toole and Krishfield, 2016). Black crosses - position of MSS profiles used for validation Schulz et al. (2022). The green polygon indicates an area with mainly straight drift trajectories, whereas the orange polygon indicates an area with often overlapping buoy trajectories. The magenta rectangle shows the area of Figure 9. b) - bold lines temperature, salinity, density, and buoyancy frequency (N^2) profiles used as initial conditions in the model; thin lines - profiles of the independent MSS data used for the model validation (see Section 3.1). c) - border situation map with the ship's drift trajectory marked in white. The buoyancy frequency is defined as $N^2 = \frac{g}{\rho}\frac{d\rho}{dz}$, where g is the acceleration of gravity, ρ the density and z the depth.

(Tippenhauer et al. (2023a)) and from a location a few hundred meters away from the ship, at the "Ocean City" (OC-CTD; 44 profiles up to 500 m) (Tippenhauer et al. (2023b)). ITP profiles with unstable stratification or a vertical range of less than 10 m were excluded from the analysis. Data from the profiles were averaged with a standard pressure interval of 1 dbar (a depth interval of about 1 m) as indicated in the data sources. The measurement accuracy of all devices is much higher compared to the error introduced by interpolation and the nudging scheme.

The observations used for model nudging covered the region between 87.6 ° East, 139.5 ° East, 84.5° North and 87.5° North, corresponding to the MOSAiC drift from October 2019 to January 2020. During the initial phase of the drift, the trajectories of the DN buoys, shown in Figure 1 by colored dots, exhibited predominantly straight paths. The later part is characterized by

the presence of overlapping and loops in the trajectories when the regional sea ice cover changed drift direction. These loops of the trajectories of different measurement platforms increase the area of the data coverage compared to the straight drift, while, at the same time, introducing ambivalence in the spatio-temporal interpretation of the data. Measured parameters could be different between data measured at the same position at different times, leading to the aliasing of the observed signal. The average ice drift speed during the observation period was 12 cm/s.

To validate the model results, we used independent temperature and salinity data from a turbulence microstructure profiler (MSS; Schulz et al., 2022). These data were not used by the model for nudging. MSS profiles were obtained at Ocean City, on a near-daily resolution, in sets of at least 3 profiles. The profiles are averaged to 1 m vertical resolution and corrected against CTD profiles, calibrated with water samples. For comparison to the model fields, we used 305 profiles (see black crosses in Figure 1).

2.5 Nudging

Model nudging was carried out assuming a quasi-steady-state, so that all observational data nudged by the model at the same model time. The model does not consider the time the observations were taken, which is a reasonable approximation at high drift speed relative to the water velocity. At the same time, we assume no significant relation of the submesoscale baroclinic structure at different ends of the model domain. Thus, nudging the model to non-time-separated observations, we get a quasi-stationary solution that can be interpreted as the result of a dynamically justified interpolation. Although in analyzing the obtained fields, it should be kept in mind that the data used for nudging are stretched over 4 months, which affects such parameters of the system as, for example, the depth of the mixed layer.

We applied a simple nudging algorithm: This method adds a nudging term to the evolution equation proportional to the difference between the model temperature and salinity, and the observational data at a given location. The full formulation of the model is given in Androsov et al. (2019). Here we present only the tracer equations in which changes have been made and where the last term represents nudging,

$$\frac{\partial \Theta_j}{\partial t} + \frac{\partial}{\partial x_i}(\mathbf{u}_i \Theta_j) + \frac{\partial}{\partial z}(w \Theta_j) = \frac{\partial}{\partial z} \vartheta_\Theta \frac{\partial \Theta_j}{\partial z} + \nabla_2 \left(K_\Theta \nabla_2 \right) \Theta_j + C_k \left(\Theta_{oj} - \Theta_j \right) \tag{3}$$

Here $i = 1, 2$, $x_1 = x$, $x_2 = y$, $u_1 = u$, and $u_2 = v$, and summation is implied over the repeating indices i; $j = 1, 2$ with $\Theta_1 = T$ and $\Theta_2 = S$ represents the potential temperature and salinity, respectively. ∇_2 is two-dimensional gradient operator. ϑ_Θ and K_Θ are the corresponding vertical and horizontal diffusion coefficients. Θ_{oj} is the observational data interpolated on mesh (see below). C_k is the spatiotemporal relaxation coefficient different for different sources of observed data, $k = 1, 2$ represents the point sources (SIT) and profiles (ITP, PS-CTD and OC-CTD). The term responsible for nudging was included only for grid nodes in the immediate vicinity of observations. To do this, a mask of nodes has been precalculated for each type of observation and is explained below. While this nudging method breaches the principle of continuity, its use is limited to distinct observational sites, rather than being uniformly applied across the entire area. This focused approach helps prevent significant issues when setting initial conditions for a free simulation.

The observed data were separated into two groups divided by the nature of these data: The first group of data was obtained using the SIT buoys. Data from these buoys have a high temporal resolution of up to 2 minutes, and a horizontal spatial resolution up to 80 m, both high compared to the temporal and spatial resolution of ITP profiles. At the same time, each buoy provided data from a maximum of 5 different depths. The second group of data comprises profiles obtained from ITP and PS/OS STD instruments.

Θ_{o1} was precalculated, and the data from the SIT buoys were interpolated onto the computational grid. Interpolation was made for two-dimensional fields for the corresponding depths of SIT buoy sensors 10,20,50,75, and 100 m. We used a modified inverse distance weighting method (Shepard, 1968) combined with fast spatial search structure kd-tree (Maneewongvatana and Mount, 1999). Interpolation was done within a maximum distance of 1 km from each observation position and a maximum number of 30 grid nodes affected by particular measurements (Figure 2 a). The rest of the mesh nodes were masked as nodes that do not participate in nudging. These up to 4 model nodes are affected by one particular observation for the model mesh with 1 km resolution. At the same time, one particular measurement affects the surrounding model mesh nodes up to 750 m away for the mesh with 250 m resolution, due to a limit of maximum of 30 nodes. When multiple data values were present, such as when the buoy trajectories intersected, a weighted average was calculated for a particular grid point (see Figure 2 b)). The interpolated 2-D fields were then used by the model for nudging. The model nudges the simulated fields to the observation fields for each of the five depths with a spread of 3 m from the observation depths (see Figure 2 c)). Thus, the spatiotemporal relaxation coefficient for SIT buoys takes the form:

$$C_1 = \begin{cases} T_{relax}/(1+0.25\cdot|Z_{obs}-Z|^2) & :|Z-Z_{obs}|\leqslant 3 \\ 0 & :|Z-Z_{obs}|>3 \end{cases} \tag{4}$$

where T_{relax} is the temporal relaxation coefficient equal to $1.1574\cdot10^{-5}\ 1/\mathrm{s}$ (one day), Z is a depth of the sigma layer, Z_{obs} is one of five depths of the CTDs at the SIT buoys. Thus, the model's nudging occurs in the vicinity of the observation point +-3 m, but the strength of the nudging decreases with distance from the observation point.

As a sensitivity study, a larger number of possible maximum values of neighboring nodes was also used. However, this does not significantly affect the final result. The total number of measurements was about 630000 for each parameter of salinity and temperature. The observational data obtained from the ITP profilers and ship-based and ocean-city CTDs were used in a similar manner.

In contrast to the SIT buoys, the model was nudged to the profiles by the PS- and OC-CTD only at the three nodes closest to the observation position (see Figure 2 d)). If more than one profile belonged to one node, then, as in the case of SIT buoys, the inverse distance weighting method was used to average the profiles. The remaining nodes of the computational grid did not participate in nudging. Vertically the model was nudged only at the horizons where the data from the profiles were present. Linear interpolation coefficients $a(z)$ and $b(z)$ were precalculated for each cell between the standard depths where observed profiles have data. The model only reads the interpolation coefficients and reconstructs the measured values at each model depth. This approach adds flexibility in setting the vertical arrangement of model sigma layers and avoids data interpolation

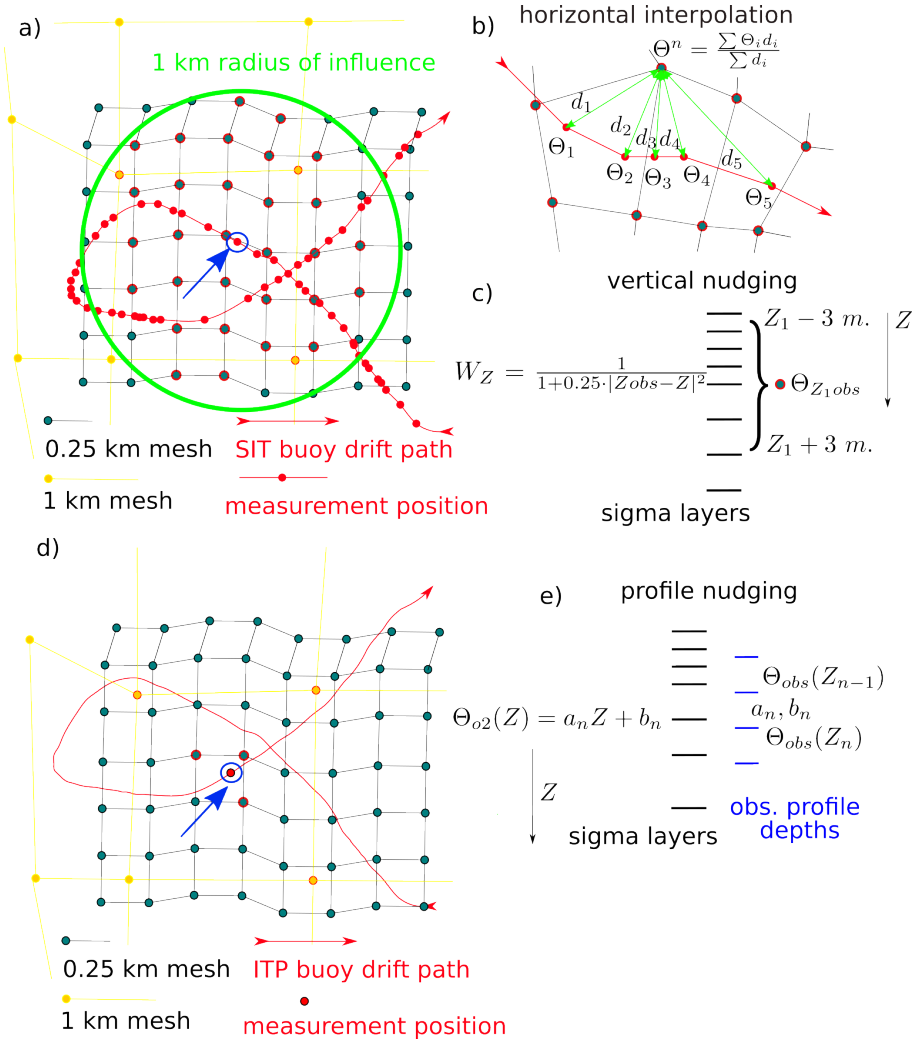

Figure 2. a), b) and c) - Schematic of interpolation and masking on the mesh. Blue and yellow circles are vertices of 0.25 and 1 km resolution meshes. The red line and circles are SIT buoy paths and measurement positions. c) - vertical relaxation weights distribution. e) - vertical interpolation of observed profile. a_n and b_n linear interpolation coefficients. Meshes vertices marked in red are influenced by the measurement marked with a blue circle.

in the process of model calculations. In this way, the spatiotemporal relaxation coefficient for profiles was $C_2 = T_{relax}$ and $\Theta_{o2} = a(z)z + b(z)$.

The significant difference in the radius of influence of the data arises from the horizontal resolution of the measurement data from the first and second groups (see prior definition). The increased radius for the SIT buoys is necessary for smoothing the fields in case of crossing the trajectories of the buoys. In the case of a small radius, this leads to artificial fronts. In the case of profiles, the probability of finding measurements at different times in one place is extremely small due to the low

frequency sampling of these instruments. SIT buoys provide data every 2 minutes, and instruments that provide incomplete vertical profiles once a day, and complete profiles at best once a week, the effect of profiles on the nudging of surface layers is significantly less. At the same time, zones deeper than 100 m are determined exclusively by profiles. It's important to note that nudging can lead to a violation of the continuity principle. However, our use of data nudging is restricted to specific observation locations, rather than being applied across the entire area. This localized application prevents significant issues from arising.

Several storm events were observed during the measurements, including one strong storm (Fang et al., 2023). Strong storms alter the dynamics nature of the surface layer and lead to ventilation of the upper ML. In the presented quasi-stationary approach, the influence of storms is considered only indirectly through changes in temperature and salinity. Therefore, the simulation results cannot reflect the dynamics during a storm. Additionally, this approach does not account for the opening of leads, which significantly affects local heat and salt fluxes. However, through nudging, the model indirectly considers these changes, albeit in a smoother manner.

2.6 Experiment description

The deep PS-CTD profile (PS122/1_10-44) conducted from *Polarstern* during November, from the surface down to the seafloor, was used as an initial condition for the whole model domain (see Figure 1 bold lines). To avoid instability in the initial conditions, the measured temperature and salinity of the surface layer were changed to constant values corresponding to a depth of 30 m. To reduce computing time, the first run was performed on the coarse mesh described in Section 2 2.3 (see Figure 3). The resulting three-dimensional temperature and salinity fields were used as initial conditions for the simulation with higher resolution. The simulation with high resolution and nudging lasted for 4 months of model time until a convergence of the numerical solution was reached. In such a way temperature and salinity differences between two successive time steps do not change significantly.

Our nudging method lead to a violation of the continuity principle and resulted in a disturbance of the velocity fields. To resolve this issue and satisfy continuity, an additional experiment was performed: A simulation with the high-resolution mesh and without nudging was run using as initial conditions the dynamical and tracer fields derived from the simulation with nudging, hereafter termed the "free run". Results of the free run are used to analyze the dynamical field that is based on the nudged run and shows a similar structure as that run constrained by the observational data while reducing the disturbance and violation of continuity, as described above.

3 Results

3.1 Model validation

The MSS data set described earlier was not used for the model nudging and serves here to validate the model with independent observations. Overall, the model is able to reproduce the lateral and vertical structure of the salinity field, as represented by the independent MSS observations (Figures 4 and 5a). Snapshots of the simulation with nudging and the free run after 2.5

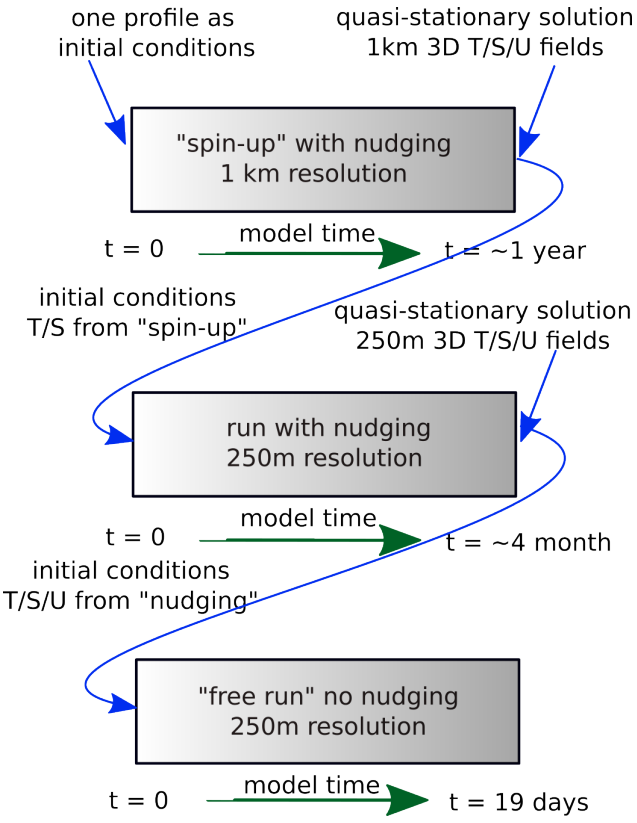

Figure 3. Schematic of conducted simulations. T/S/U are abbreviations for temperature, salinity, and velocity. The rectangles represent individual simulations.

days (Figure 4 b, c) show similar lateral salinity gradients in the ML. After 19 days in the free run (Figure 4 d)) the lateral salinity gradient is smaller due to vertical and horizontal mixing. Salinity and temperature variability is slightly lower in the model compared to the observations (Figure 5c). The maximum deviation of the model from the observations is at the depths of the maximum vertical gradients in salinity (at about 37 m) and in temperature (at about 150 m depth). Variability of salinity decreases with time in the free run, when nudging is no longer taking on the role of external forcing. In the absence of nudging the model tends to dissolve eddies and slump fronts resulting in the smoothing of lateral gradients.

The statistics of the comparison between model and SIT buoy data (Table 1) show that the model deviates from the observations despite nudging with observational data. The largest deviation is at the positions where buoy trajectories intercept each other. In such cases, the model points are aligned with at least two separate observations of the same variable at the same location, highlighting the limitations of the quasi-stationary approximation assumption. Typically, the model strives to replicate the smoothed values derived from these overlapping observations. Moreover, the horizontal resolution of the SIT buoy observations is often higher than the spacing of the model grid, which results in larger differences between individual observed values and model output, as one model grid point covers several observations in space. The root mean square errors

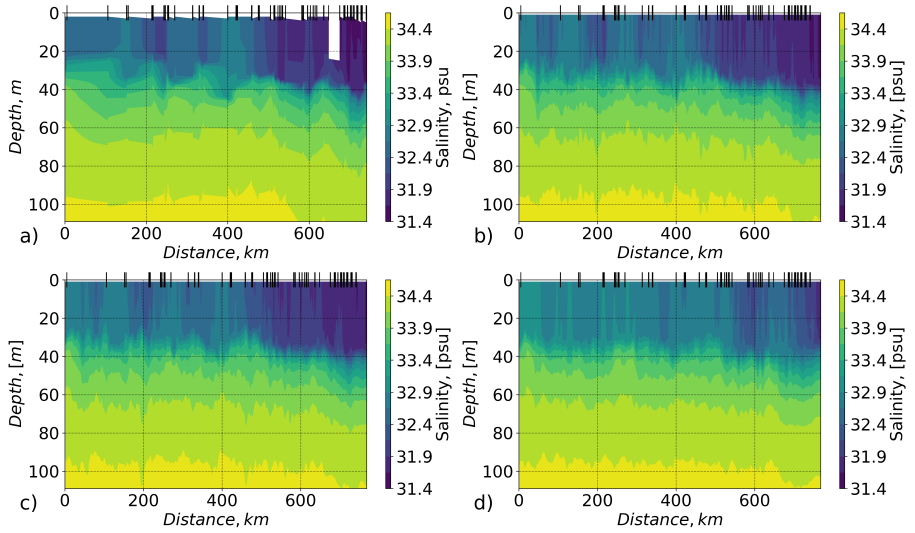

Figure 4. Salinity in the upper 120 m along the ship drift path. The x-axis shows the distance of the ship drift with 0 km at the position of the first MSS profile. Positions of the MSS profiles are marked by black vertical lines at the top axes. a) - salinity measured by the MSS profiler (Schulz et al., 2022) at Ocean City in vicinity of the ship. Here linear interpolation between MSS casts has been applied. b),c) and d) - modeled salinity at the ship positions: a) - simulation with nudging. b) - free run, 2.5 days after nudging was stopped. c) free run, 19 days after nudging was stopped.

Table 1. Root mean square error (RMSe) between measured by SIT buoys and modeled salinity/temperature and standard deviation (SD) of both at different depths.

depth	RMSe nudging	SD nudging	RMSe free run	SD free run	SD SIT
10	0.29 / 0.01	0.34 / 0.02	0.37 / 0.02	0.35 / 0.02	0.4 / 0.02
20	0.37 / 0.02	0.34 / 0.02	0.44 / 0.02	0.35 / 0.02	0.38 / 0.02
50	0.08 / 0.02	0.2 / 0.02	0.1 / 0.02	0.19 / 0.02	0.23 / 0.03
75	0.03 / 0.07	0.06 / 0.09	0.04 / 0.09	0.06 / 0.08	0.08 / 0.12
100	0.02 / 0.1	0.03 / 0.15	0.02 / 0.13	0.02 / 0.14	0.03 / 0.19

(RMSe) are in the range of the standard deviation (SD) of the model and the observations in the surface ML (Table 1). RMSe significantly decreases for salinity underneath the halocline and about half of the SD in observation. At the same time, RMSe and SD increase for temperature underneath the halocline where temperature gradients increase (not shown).

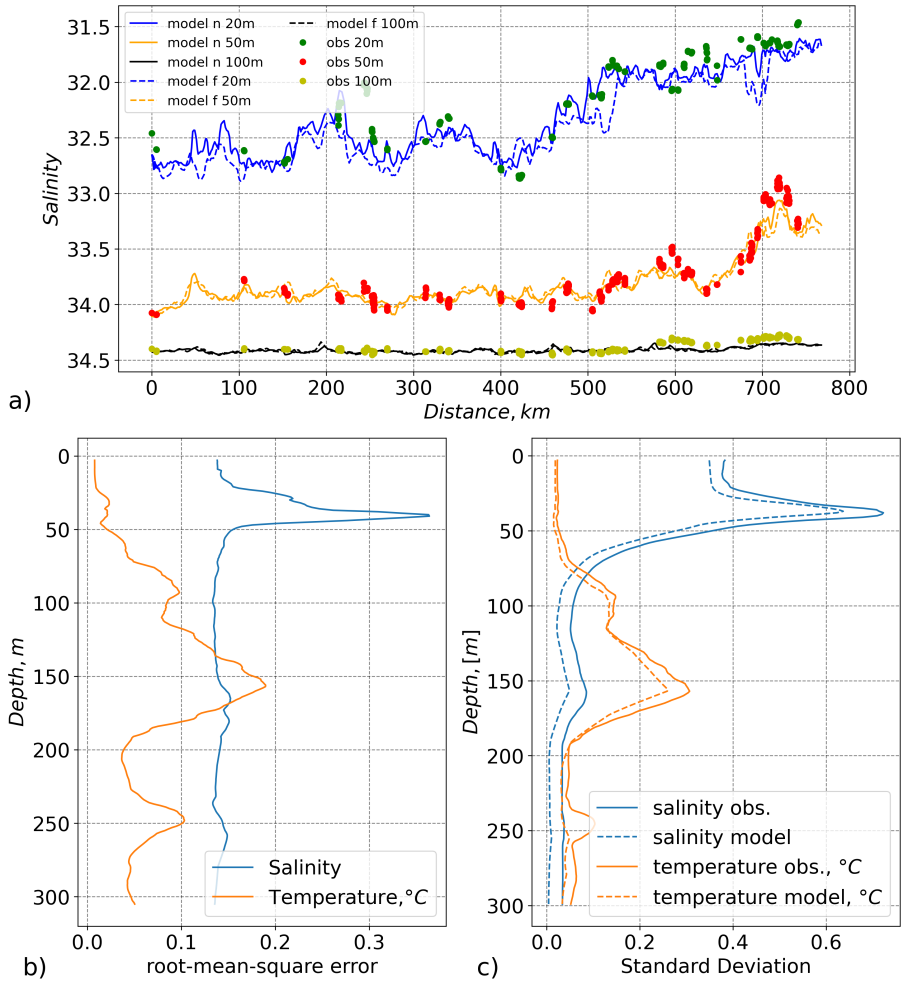

Figure 5. a) - salinity at the three depths 20,50 and 100 m. Y-axis is inverted. Coloured dots - observed salinity data (MSS) from 10 (green), 50 (red), and 100 (orange) m depth. Coloured lines – modeled salinity extracted at ship positions. Solid lines - model with nudging, dashed lines - free run after 2.5 days. b) - Standard deviation, blue line - observations, orange - model with nudging. c) - root mean square error of model data in comparison to observational data (MSS).

3.2 T/S reconstruction

Cross sections along 115 °N and 86.2 °E in the modeled fields (Figure 6) indicate a decrease in ML salinity and density towards the north of similar order as the smaller-scale spatial variability. The ML depth varies from about 36 in the south to 40 in the north with a minimum of 32 m, resulting in a gradient of 0.014 m/km with 0.6 m/km standard deviation. The density in the ML, likewise, changed for about 1.1 kg/m^3. Underneath the halocline, isopycnal lines slope by more than 10 m along the section with less smaller-scale variability than at the bottom of the ML. In the west-east direction the ML depth increases amid less

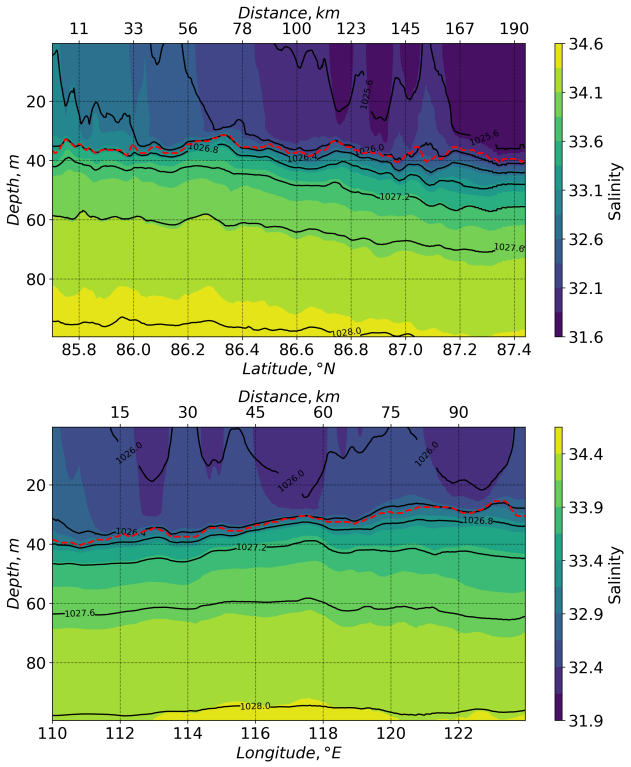

Figure 6. Cross sections along 115 °North Longitude (upper) and 86.2 °East Latitude (lower). Filled colour contours are salinity psu, and black contours are density $\mathrm{kg/m^3}$. Red dashed lines show ML depth.

small-scale variability than seen in the north-south section. Both sections reveal an increase in the Mixed Layer (ML) depth from northwest to southeast. However, the slope of the isopycnals from west to east is less consistent below approximately 40 m compared to the north-south section. The same standard deviation in ML depth characterizes both directions. ML depth changes from 27 to 40 m from east to west with a mean gradient of -0.084 m/km and 0.6 m/km gradient standard deviation. Whereas the ML low-salinity (high-density) intrusions from the surface could be associated with both changes in surface heat and salt fluxes in reality, here effected through the nudging the submesoscale variability of the ML depth is most likely governed by the eddy dynamics.

4 Discussion

4.1 Eddy kinetic energy

Commonly, modeled eddy kinetic energy (EKE) is defined as the difference between total kinetic energy and mean kinetic energy (Wang et al., 2020). The current setup has no external forcing other than nudging to data. In the absence of any external

forcing, the model does not produce significant mean velocity, resulting in negligible mean kinetic energy. Therefore, the total kinetic energy is mainly defined by the anomaly in the velocity and linked to eddies. The EKE is calculated here as

$$EKE = (u^2 + v^2)/2. \tag{5}$$

The EKE is decreasing in the free run with time due to dissipating eddies, as an effect of surface friction or numerical diffusion, for example. The absence of a mechanism to generate new EKE (and new eddies) leads to a decrease in the free run, whereas eddies that formed in the run with nudging remain in the free run for more than 20 days. Figure 7 indicates enhanced modeled EKE activity within two separate depth ranges, both of which are around maxima in N^2 (as defined in Figure 1): one in the halocline and the other in the warm Atlantic Water. Similar vertical distributions of EKE in the ice-covered central Arctic basins have been observed previously by Meneghello et al. (2021) and modeled by Wang et al. (2020), and such a bimodal distribution of eddies was discussed in detail by Zhao et al. (2014). However, the data only cover part of the winter, so we cannot analyze the effects of seasonal variability and the associated ice conditions on the distribution of eddies. Throughout the entire time of the measurements used here, the ice cover was already formed and consolidated with only a limited number of small openings (Nicolaus et al. (2022)).

We can see a difference in the distribution of our modeled EKE: in the southern part of the domain, the maximum energy was around the warm Atlantic Water, whereas in the northern part, it was intensified in the halocline, just underneath the surface ML. The latter is associated with stronger stratification due to high salinity gradients. In the northern part of the considered domain there were sharp changes in the direction of the ice drift, which, in turn, also affected the salinity distribution of the near-surface waters. Here it should be noted that the northern part is covered by data with many overlaps in the drift trajectories (orange polygon in Figure 1 and 7). This, on the one hand, leads to the smoothing of the fields in the model compared to observations where trajectories intersect. On the other hand, it can lead to the appearance of local fronts at submesoscales during nudging. Using a free run partially removes the latter problem.

4.2 Eddy examples

The velocity structure remains similar during 19 days of the free run (see Figure 8), and most of the eddies changing shape and intensity remain close to where they formed. The number of eddies formed in the model during the fairly fast and straight drift is similar to that in the area with overlapping drift trajectories. Most eddies travel much slower than the drift of the ship in the area where the peak in EKE can be seen in the warm Atlantic Water.

The eddy dynamics differ between the northern and southern parts of our region of interest: A few of the small-scale eddies and filaments formed at the depth of the halocline dissipate within a few days in the free run. Among the remaining, there are those that actively travel and interact with each other. Figure 9 shows an example of a simulated anticyclonic eddy with negative relative vorticity that, during the free run, travels and interacts with a bigger size cyclonic eddy (positive relative vorticity). The anticyclonic eddy is situated between 30 and 90 m deep and about 5 km in diameter. The cyclonic eddy is slightly larger and changes its horizontal dimensions from 7 to 10 km. The anticyclonic eddy has clearly defined contours, in contrast to

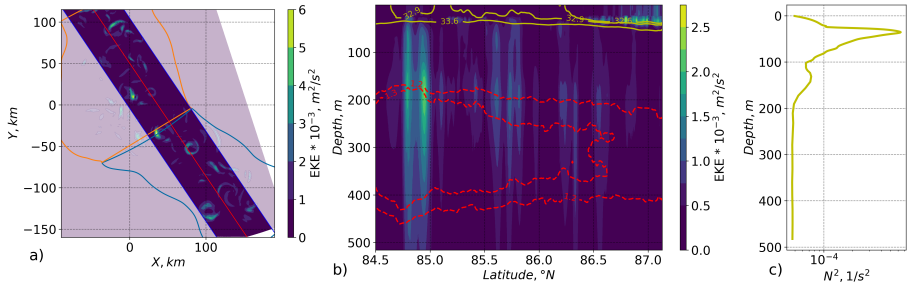

Figure 7. Modeled eddy kinetic energy and N^2 after 5 days of free run. a) - EKE at 47 m depth. Highlighted area indicating averaging area in the stereographic projection. Area of averaging is chosen in such a way that the length of the line along the X direction is the same for any Y position. Averaging was done along X direction and covered 80 km with the center indicated by the red line. The red line was chosen in such a way that it is the longest straight line within the area covered by data. Green and orange polygons indicate the same areas as in Figure 1. b) - vertical distribution of the averaged along X direction EKE. Red dashed lines are isotherms for 1.2 and 1.3 °C. Yellow solid lines are isohalines for 33.6 and 32.9 psu. c) panel shows mean stratification computed over the area shown in panel a).

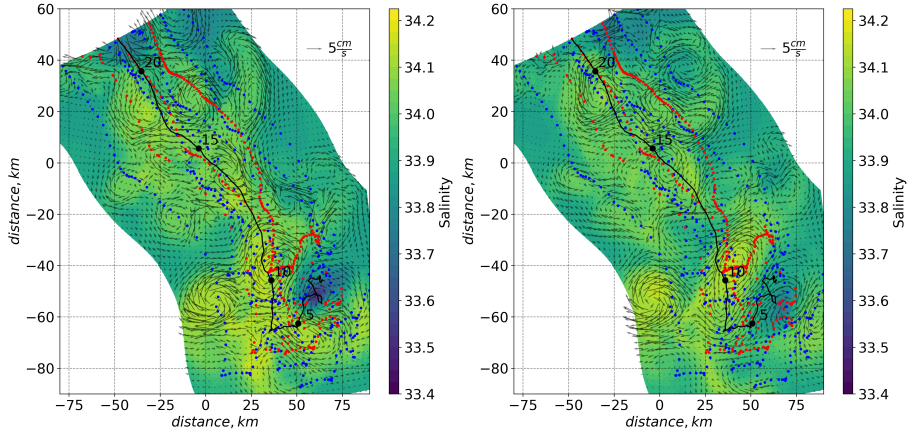

Figure 8. Salinity at 47 m depth in the free run after 5 (left) and 19 (right) days model time, with velocity vectors (arrow top right indicate 5 $\mathrm{cm/s}$) zoomed to the area with mainly straight drift (indicated by a green contour in Figure 1). The black line indicates the drift track of *Polarstern*. The black dots are the daily positions of the ship.

the cyclonic one with more diffuse boundaries. The maximum velocities within the eddies reach 12 $\mathrm{cm/s}$. The anticyclonic eddy first travels in the direction of the cyclonic eddy, then circumvents it. The cyclonic eddy remains in position before the anticyclonic eddy approaches it, but once they meet the cyclonic eddy begins to stretch towards the anticyclonic one. Changing shape the cyclonic eddy starts to move north as a result of the two eddies interacting. The center of the cyclonic eddy moved a total of about 7 km over 19 days. The anticyclonic eddy starts to spin around the cyclonic one and increased in translation speed. On its way, it changes shape from almost a circle to an elongated ellipse and back several times depending on its relative position to the anticyclone eddy.

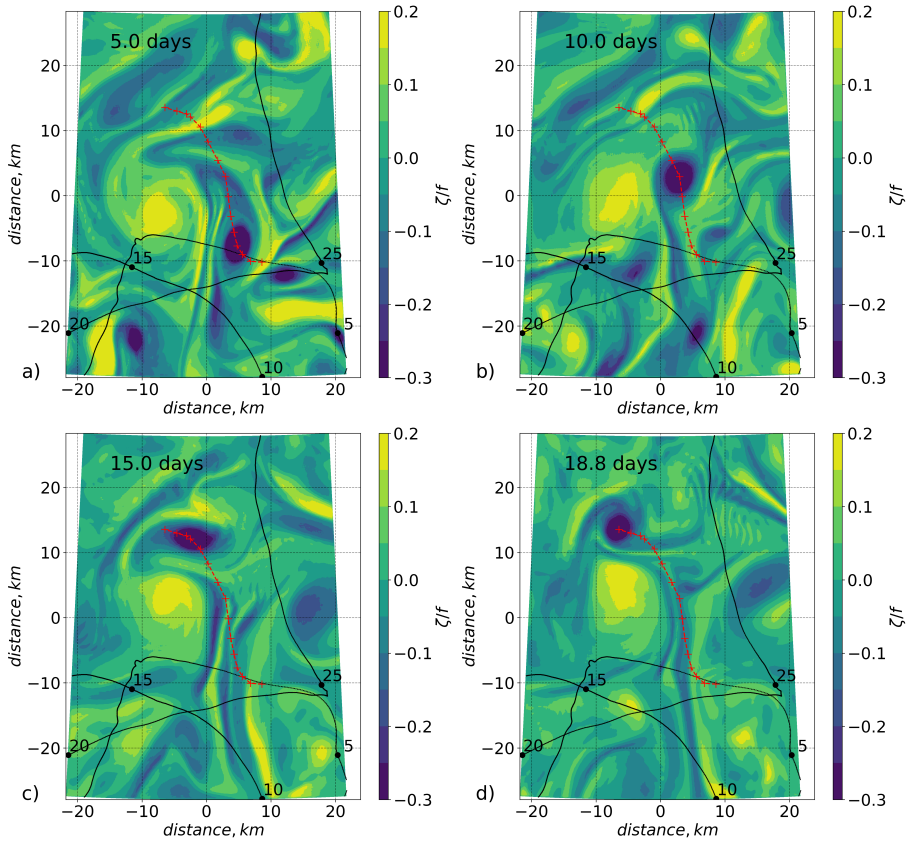

Figure 9. Snapshots of relative vorticity at 47 m depth in the free run. The depth of the ML depth is about 27 m. a),b),d), and c) - snapshots after 5,10,15, and 18.8 days of model time, respectively. The black line indicates the drift track of *Polarstern*. The black dots are the daily positions of the ship starting 2019-11-12. The red dashed line shows the trajectory of the center of the anticyclonic eddy described in the text, where the center was identified by eye. The position of the region shown in this figure is denoted by the cyan box in Figure 1.

This example demonstrates that the interpretation of unevenly distributed observational data, sometimes overlapping in space at different times (buoy drift trajectory loops), is complicated, but that the drifting buoy obsevations were able to capture the cyclonic eddy. This is due to the quasi-steady nature of the eddy during the time the when drift passed this geographic position. The development of the fast-traveling anticyclonic eddy could not be measured entirely by the DN, as the speed of the eddy was not aligned with the drift of the buoys. At the same time, the distances between the buoys are larger than the eddy core diameters in our model, which would lead to a misinterpretation during analyzing such data by common interpolation methods. This generally applies to the DN measurements, as we only obtained a snapshot in space and time with the DN observing over the scales set by the different DN sites.

The features of the dynamical field structure of the northern and southern parts are different. This can be explained by the nature of the ice drift. Mahadevan et al. (2010) have shown that submesoscale near-surface eddies are dissipating faster under

constant unidirectional drift, something that could have happened in the southern part. At the same time, the ice drift has practically no effect on eddies without a dynamic connection to the surface, e.g. within the halocline or the warm Atlantic Water. The ice drift constantly changed direction in the northern part, and at the same time, horizontal density gradients were observed in the surface layer. Near-surface vortices are more likely to form in such conditions. In the northern part, the ice drift changes direction, but the model forcing remained constant. However, data coverage is more comprehensive where the ice drift is sinuous. This implies that data sampling influences the simulation of vortices, which are expected to be more prevalent in the upper portion of the graphs.

4.3 Limitations of our method

Changes in the flows due to atmospheric influences are exclusively accounted for through nudging, which is determined by the density of the data and shows a smoothed pattern. In the quasi-stationary case, considering that the used observational data have a temporal spread of several months, this can result in the appearance of horizontal gradients in temperature and salinity fields. For example, we can expect a decrease in temperature and an increase in salinity in the mixed layer due to ice formation in the temporal range from November to January. Considering that the buoy drift was northwest during this time, with such a quasi-stationary approach, we can expect an increase in salinity and density in the mixed layer in the north and west directions. However, according to the simulation results, we observe the opposite pattern: no gradient in the west-east direction and a reverse gradient from north to south (see Section 3.2). Thus, it can be assumed that the instantaneous gradient (a gradient that could be measured at a single point in time) in the north-south direction is more significant than in the reconstruction.

Despite significantly reducing the influence of regional boundaries on the final solution through increased model resolution, there remains an "internal boundary" in the model between regions with available data and regions without observations. This creates an artificial front between these two areas, determined by the initial conditions. Instabilities can occur along the boundary of this front due to the dynamics in the data-rich area and the absence of dynamics in the data-sparse area. This issue is partially mitigated by conducting a long spin-up calculation on a coarse grid, which significantly smooths the front between the areas.

In our simulations, there are no barotropic currents or currents caused by baroclinic gradients on the scales of the Arctic basins. Typical time averaged velocities for such currents can be 2-5 cm/s (Rudels, 2009). In situ velocity measurements during the MOSAiC experiment show average velocity values of about 3 cm/s at depths of 60-200 m (Figure 11 in Rabe et al., 2022; Baumann et al., 2021). The average velocity values across the entire area for same depth in our simulations range from 1-2 cm/s depending on the depth, with peaks up to 15 cm/s in eddies. Thus, we can assume that the influence of basin-scale dynamics not considered in our work has a relatively minor effect on the final solution. In future work, it would be worthwhile to use ocean and atmosphere reanalysis data (which utilize MOSAiC data) to provide initial and boundary conditions, if and when they become available. Despite the coarse vertical and horizontal resolutions of these reanalyses, their usage would allow transitioning from a quasi-stationary case to a time-dependent solution.

5 Summary

The MOSAiC project has collected a rich data set of physical oceanography observations in the central Arctic. Various measurement techniques and tools make combining and analyzing the obtained data challenging. This paper presents ocean model reanalyses of the first part of the MOSAiC field campaign during winter. Three-dimensional temperature and salinity fields were reconstructed by model nudging to the observed data. The model setup covers the Arctic region bounded by 84.5°to 87.5°North and 87.6°to 139.5°East which corresponds to the MOSAiC drift from October 2019 to January 2020. Using the regional FESOM-C model has allowed us to analyze the dynamic fields.

The model was further developed to suit our needs. The turbulence closure was adapted specifically for this work by modification of the turbulence scale. Further, we extended the model with a semi-implicit method to calculate the sea level. The model code was parallelized with MPI libraries, which made it possible to perform calculations with the required resolution and 1.3 million horizontal nodes. Considering 240 vertical layers for the current setup, the number of calculated model points is more than three times that of the eddy-permitting global mesh with a quasi-uniform resolution of 15 km in the FESOM2 setup (Danilov et al., 2017). Our developed setup of the FESOM-C model with an unstructured mesh makes it possible to mitigate the influence of boundary conditions on the area of interest. Near-surface and deep submesoscale processes are resolved by the high horizontal resolution of up to 250 m and the vertical resolution of up to 1 m. A simple algorithm was developed to nudge the model to the observed data, that makes it possible to use a large amount of data from different measuring systems. More than 630,000 single-point temperature and salinity observations and over a thousand vertical profiles were nudged by the model.

We validate the model output against independent data that were not used for nudging and the vertical and horizontal distributions of temperature and salinity are well reproduced by the model. The main discrepancies between independent and modeled data are at the intersections of the drift trajectories of the buoys. Buoys have overlapping tracks due to the ice drift loops, for example, during rapid changes in the wind direction. These not-quite-synoptic measurements lead to a gridded (nudging) field that is not necessarily equal to individual observed values as a result of the weighted mean interpolation. These crossing points could be utilized as temporal references to calculate errors associated with the 'quasi-stationary' assumption in future publications concerning these data and the model.

By employing the model nudging to data method along with a model free run we have been able to reconstruct dynamically consistent three-dimensional temperature, salinity, and density fields. The results of our simulation allow analyzing the horizontal and vertical distribution of temperature, salinity, and velocity on a regular grid. Our analysis of the dynamic characteristics reveals the existence of two separate depth ranges of enhanced eddy kinetic energy located around two maxima in buoyancy frequency in the central Arctic basins. This bimodal distribution of eddies, previously noted in various studies, shows regional variations: in the southern domain, maximum energy is near the warm Atlantic Water, while in the northern part, it's intensified in the halocline beneath the surface mixed layer. The model resolves several stationary warm-Atlantic-Water eddies and provides insights into the associated dynamics that would not be possible by analyzing the observations alone.

Code and data availability. The FESOM-C code and model setup used in this study can be found under DOI:https://doi.org/10.5281/zenodo.8004904. Modelling results for 6 vertical layers and 5 temporal layers of the free run created during this study is openly available in the Zenodo open data repository and can also be found at the provided link. Rest of the modelling data are available upon request by contacting the corresponding authors.

Author contributions. IK, BR, YCF and AA were responsible for the initial conceptualization of the study. IK developed the model nudging method, model setup, simulations, processing the results and wrote the paper with a strong contribution from BR and AA. Providing, post processing and the curation the observational data, deploying the instruments in the field: BR, YCF, MH, IK, AQZ, ST, KS, VM, IF, MJ. AA, IK, SH, VF developing the FESOM-C code. All co-authors reviewed the manuscript and contributed to the writing and final editing.

Competing interests. Ilker Fer is a member of the editorial board of Ocean Science.

Acknowledgements. Data presented in this paper were produced as part of the international Multidisciplinary drifting Observatory for the Study of the Arctic Climate (MOSAiC) with the tag MOSAiC20192020 (grant numbers AWI_PS122_00 and AFMOSAiC-1_00). The instruments were funded as part of the MIDO (Multidisciplinary Ice-based Drifting Observatory) infrastructure. The study contributes to the Changing Arctic Ocean (CAO) program, jointly funded by the UKRI Natural Environment Research Council (NERC) and the BMBF, project Advective Pathways of nutrients and key Ecological substances in the ARctic (APEAR) grants NE/R012865/1, NE/R012865/2 and #03V01461; the project EPICA in the research theme MARE:N - Polarforschung/MOSAiC funded by the German Federal Ministry for Education and Research with funding number 03F0889A; the European Commission for EU H2020 grant no. 101003472 (project Arctic PASSION), and the AROMA (Arctic Ocean mixing processes and vertical fluxes of energy and matter) project by the Research Council of Norway, grant number 294396. We thank the administrators of the AWI cluster Ollie and Albedo, where the simulations took place, for their continual support and patience. Full acknowledgments are available in Nixdorf et al. (2021).

References

Androsov, A., Rubino, A., Romeiser, R., and Sein, D. V.: Open-ocean convection in the Greenland Sea: preconditioning through a mesoscale chimney and detectability in SAR imagery studied with a hierarchy of nested numerical models, Meteorologische Zeitschrift, 14, 693–702, https://doi.org/10.1127/0941-2948/2005/0078, 2005.

Androsov, A., Nerger, L., Schnur, R., Schröter, J., Albertella, A., Rummel, R., Savcenko, R., Bosch, W., Skachko, S., and Danilov, S.: On the assimilation of absolute geodetic dynamic topography in a global ocean model: impact on the deep ocean state, Journal of Geodesy, 93, 141–157, https://doi.org/10.1007/s00190-018-1151-1, 2018.

Androsov, A., Fofonova, V., Kuznetsov, I., Danilov, S., Rakowsky, N., Harig, S., Brix, H., and Helen Wiltshire, K.: FESOM-C v.2: Coastal dynamics on hybrid unstructured meshes, Geoscientific Model Development, 12, 1009–1028, https://doi.org/10.5194/gmd-12-1009-2019, 2019.

Androsov, A., Boebel, O., Schröter, J., Danilov, S., Macrander, A., and Ivanciu, I.: Ocean Bottom Pressure Variability: Can It Be Reliably Modeled?, Journal of Geophysical Research: Oceans, 125, https://doi.org/10.1029/2019JC015469, 2020.

Barth, A., Beckers, J.-M., Troupin, C., Alvera-Azcárate, A., and Vandenbulcke, L.: divand-1.0: <i>n</i>-dimensional variational data analysis for ocean observations, Geoscientific Model Development, 7, 225–241, https://doi.org/10.5194/gmd-7-225-2014, 2014.

Baumann, T., Fer, I., Bryhni, H., Peterson, A. K., Allerholt, J., Fang, Y.-C., Hoppmann, M., Karam, S., Koenig, Z., Kong, B., Mohrholz, V., Muilwijk, M., Schaffer, J., Schulz, K., Sukhikh, N., and Tippenhauer, S.: Under-ice current measurements during MOSAiC from a 75 kHz acoustic Doppler profiler, https://doi.org/10.1594/PANGAEA.934792, 2021.

Bretherton, F. P., Davis, R. E., and Fandry, C. B.: A technique for objective analysis and design of oceanographic experiments applied to MODE-73, Deep Sea Research and Oceanographic Abstracts, 23, 559–582, https://doi.org/http://dx.doi.org/10.1016/0011-7471(76)90001-2, 1976.

Courtier, P., Thépaut, J.-N., and Hollingsworth, A.: A strategy for operational implementation of 4D-Var, using an incremental approach, Quarterly Journal of the Royal Meteorological Society, 120, 1367–1387, https://doi.org/10.1002/qj.49712051912, 1994.

Danilov, S. and Androsov, A.: Cell-vertex discretization of shallow water equations on mixed unstructured meshes, Ocean Dynamics, 65, 33–47, https://doi.org/10.1007/s10236-014-0790-x, 2015.

Danilov, S., Sidorenko, D., Wang, Q., and Jung, T.: The Finite-volumE Sea ice–Ocean Model (FESOM2), Geoscientific Model Development, 10, 765–789, https://doi.org/10.5194/gmd-10-765-2017, 2017.

Della Penna, A. and Gaube, P.: Overview of (Sub)mesoscale Ocean Dynamics for the NAAMES Field Program, Frontiers in Marine Science, 6, 384, https://doi.org/10.3389/fmars.2019.00384, 2019.

Dmitrenko, I. A., Kirillov, S. A., Ivanov, V. V., and Woodgate, R. A.: Mesoscale Atlantic water eddy off the Laptev Sea continental slope carries the signature of upstream interaction, Journal of Geophysical Research: Oceans, 113, https://doi.org/10.1029/2007JC004491, 2008.

Fang, Y.-C., Rabe, B., Kuznetsov, I., Hoppmann, M., Tippenhauer, S., Regnery, J., He, H., and Li, T.: Early winter upper-ocean variability in the Amundsen Basin of the Arctic Ocean from the MOSAiC expedition, Earth System Science Data, submitted to Elementa, 2023.

Fofonova, V., Androsov, A., Sander, L., Kuznetsov, I., Amorim, F., Hass, H. C., and Wiltshire, K. H.: Non-linear aspects of the tidal dynamics in the Sylt-Rømø Bight, south-eastern North Sea, Ocean Science, 15, 1761–1782, https://doi.org/10.5194/os-15-1761-2019, 2019.

Gula, J., Taylor, J., Shcherbina, A., and Mahadevan, A.: Chapter 8 - Submesoscale processes and mixing, in: Ocean Mixing, edited by Meredith, M. and Naveira Garabato, A., pp. 181–214, Elsevier, https://doi.org/10.1016/B978-0-12-821512-8.00015-3, 2022.

Hoppmann, M., Kuznetsov, I., Fang, Y.-C., and Rabe, B.: Mesoscale observations of temperature and salinity in the Arctic Transpolar Drift: a high-resolution dataset from the MOSAiC Distributed Network, Earth System Science Data Discussions, 2022, 1–33, https://doi.org/10.5194/essd-2022-66, 2022.

Hordoir, R., Skagseth, Ø., Ingvaldsen, R. B., Sandø, A. B., Löptien, U., Dietze, H., Gierisch, A. M. U., Assmann, K. M., Lundesgaard, Ø., and Lind, S.: Changes in Arctic Stratification and Mixed Layer Depth Cycle: A Modeling Analysis, Journal of Geophysical Research: Oceans, 127, https://doi.org/10.1029/2021JC017270, 2022.

Krumpen, T. and Sokolov, V.: The Expedition AF122/1 : Setting up the MOSAiC Distributed Network in October 2019 with Research Vessel AKADEMIK FEDOROV, techreport, Berichte zur Polar- und Meeresforschung = Reports on polar and marine research, Alfred Wegener Institute for Polar and Marine Research, Bremerhaven, https://doi.org/10.2312/BzPM_0744_2020, 2020.

Kuznetsov, I., Androsov, A., Fofonova, V., Danilov, S., Rakowsky, N., Harig, S., and Wiltshire, K. H.: Evaluation and Application of Newly Designed Finite Volume Coastal Model FESOM-C, Effect of Variable Resolution in the Southeastern North Sea, Water, 12, https://doi.org/10.3390/w12051412, 2020.

Li, J., Liao, W.-k., Choudhary, A., Ross, R., Thakur, R., Gropp, W., Latham, R., Siegel, A., Gallagher, B., and Zingale, M.: Parallel NetCDF: A High-Performance Scientific I/O Interface, in: Proceedings of the 2003 ACM/IEEE Conference on Supercomputing, SC '03, p. 39, Association for Computing Machinery, New York, NY, USA, https://doi.org/10.1145/1048935.1050189, 2003a.

Li, Z., Saad, Y., and Sosonkina, M.: pARMS: a parallel version of the algebraic recursive multilevel solver, Numerical Linear Algebra with Applications, 10, 485–509, https://doi.org/https://doi.org/10.1002/nla.325, 2003b.

Llinás, L., Pickart, R. S., Mathis, J. T., and Smith, S. L.: Zooplankton inside an Arctic Ocean cold-core eddy: Probable origin and fate, Deep Sea Research Part II: Topical Studies in Oceanography, 56, 1290–1304, https://doi.org/10.1016/j.dsr2.2008.10.020, the Western Artic Shelf-Basin Interactions (SBI)Project, Vol.2, 2009.

Lyu, G., Serra, N., Zhou, M., and Stammer, D.: Arctic sea level variability from high-resolution model simulations and implications for the Arctic observing system, Ocean Science, 18, 51–66, https://doi.org/10.5194/os-18-51-2022, 2022.

Mahadevan, A.: The Impact of Submesoscale Physics on Primary Productivity of Plankton, Annual Review of Marine Science, 8, 161–184, https://doi.org/10.1146/annurev-marine-010814-015912, 2016.

Mahadevan, A., Tandon, A., and Ferrari, R.: Rapid changes in mixed layer stratification driven by submesoscale instabilities and winds, Journal of Geophysical Research, 115, https://doi.org/10.1029/2008JC005203, 2010.

Maneewongvatana, S. and Mount, D.: It's okay to be skinny, if your friends are fat, Center for Geometric Computing 4th Annual Workshop on Computational Geometry, 1999.

Manucharyan, G. E. and Thompson, A. F.: Submesoscale Sea Ice-Ocean Interactions in Marginal Ice Zones, Journal of Geophysical Research: Oceans, 122, 9455–9475, https://doi.org/10.1002/2017JC012895, 2017.

Marcinko, C. L. J., Martin, A. P., and Allen, J. T.: Characterizing horizontal variability and energy spectra in the scpA/scp rctic scpO/scp cean halocline, Journal of Geophysical Research: Oceans, 120, 436–450, https://doi.org/10.1002/2014JC010381, 2015.

Maslowski, W., Kinney, J. C., Marble, D. C., and Jakacki, J.: Towards Eddy-Resolving Models of the Arctic Ocean, pp. 241–264, American Geophysical Union (AGU), https://doi.org/10.1029/177GM16, 2008.

Meneghello, G., Marshall, J., Lique, C., Isachsen, P. E., Doddridge, E., Campin, J.-M., Regan, H., and Talandier, C.: Genesis and Decay of Mesoscale Baroclinic Eddies in the Seasonally Ice-Covered Interior Arctic Ocean, Journal of Physical Oceanography, 51, 115 – 129, https://doi.org/10.1175/JPO-D-20-0054.1, 2021.

Mensa, J. A. and Timmermans, M.-L.: Characterizing the seasonal cycle of upper-ocean flows under multi-year sea ice, Ocean Modelling, 113, 115–130, https://doi.org/10.1016/j.ocemod.2017.03.009, 2017.

Mogensen, K., Alonso-Balmaseda, M., Weaver, A., Martin, M., and Vidard, A.: NEMOVAR: A variational data assimilation system for the NEMO ocean model, https://doi.org/10.21957/3yj3mh16iq, 2009.

Neder, C., Fofonova, V., Androsov, A., Kuznetsov, I., Abele, D., Falk, U., Schloss, I. R., Sahade, R., and Jerosch, K.: Modelling suspended particulate matter dynamics at an Antarctic fjord impacted by glacier melt, Journal of Marine Systems, 231, 103 734, https://doi.org/10.1016/j.jmarsys.2022.103734, 2022.

Nerger, L., Tang, Q., and Mu, L.: Efficient ensemble data assimilation for coupled models with the Parallel Data Assimilation Framework: example of AWI-CM (AWI-CM-PDAF 1.0), Geoscientific Model Development, 13, 4305–4321, https://doi.org/10.5194/gmd-13-4305-2020, 2020.

Nicolaus, M., Perovich, D. K., Spreen, G., Granskog, M. A., von Albedyll, L., Angelopoulos, M., Anhaus, P., Arndt, S., Belter, H. J., Bessonov, V., Birnbaum, G., Brauchle, J., Calmer, R., Cardellach, E., Cheng, B., Clemens-Sewall, D., Dadic, R., Damm, E., de Boer, G., Demir, O., Dethloff, K., Divine, D. V., Fong, A. A., Fons, S., Frey, M. M., Fuchs, N., Gabarró, C., Gerland, S., Goessling, H. F., Gradinger, R., Haapala, J., Haas, C., Hamilton, J., Hannula, H.-R., Hendricks, S., Herber, A., Heuzé, C., Hoppmann, M., Høyland, K. V., Huntemann, M., Hutchings, J. K., Hwang, B., Itkin, P., Jacobi, H.-W., Jaggi, M., Jutila, A., Kaleschke, L., Katlein, C., Kolabutin, N., Krampe, D., Kristensen, S. S., Krumpen, T., Kurtz, N., Lampert, A., Lange, B. A., Lei, R., Light, B., Linhardt, F., Liston, G. E., Loose, B., Macfarlane, A. R., Mahmud, M., Matero, I. O., Maus, S., Morgenstern, A., Naderpour, R., Nandan, V., Niubom, A., Oggier, M., Oppelt, N., Pätzold, F., Perron, C., Petrovsky, T., Pirazzini, R., Polashenski, C., Rabe, B., Raphael, I. A., Regnery, J., Rex, M., Ricker, R., Riemann-Campe, K., Rinke, A., Rohde, J., Salganik, E., Scharien, R. K., Schiller, M., Schneebeli, M., Semmling, M., Shimanchuk, E., Shupe, M. D., Smith, M. M., Smolyanitsky, V., Sokolov, V., Stanton, T., Stroeve, J., Thielke, L., Timofeeva, A., Tonboe, R. T., Tavri, A., Tsamados, M., Wagner, D. N., Watkins, D., Webster, M., and Wendisch, M.: Overview of the MOSAiC expedition: Snow and sea ice, Elementa: Science of the Anthropocene, 10, https://doi.org/10.1525/elementa.2021.000046, 2022.

Nishino, S., Kawaguchi, Y., Fujiwara, A., Shiozaki, T., Aoyama, M., Harada, N., and Kikuchi, T.: Biogeochemical Anatomy of a Cyclonic Warm-Core Eddy in the Arctic Ocean, Geophysical Research Letters, 45, 11,284–11,292, https://doi.org/10.1029/2018GL079659, 2018.

Nixdorf, U., Dethloff, K., Rex, M., Shupe, M., Sommerfeld, A., Perovich, D. K., Nicolaus, M., Heuzé, C., Rabe, B., Loose, B., Damm, E., Gradinger, R., Fong, A., Maslowski, W., Rinke, A., Kwok, R., Spreen, G., Wendisch, M., Herber, A., Hirsekorn, M., Mohaupt, V., Frickenhaus, S., Immerz, A., Weiss-Tuider, K., König, B., Mengedoht, D., Regnery, J., Gerchow, P., Ransby, D., Krumpen, T., Morgenstern, A., Haas, C., Kanzow, T., Rack, F. R., Saitzev, V., Sokolov, V., Makarov, A., Schwarze, S., Wunderlich, T., Wurr, K., and Boetius, A.: MOSAiC Extended Acknowledgement, https://doi.org/10.5281/zenodo.5541624, 2021.

Nurser, A. J. G. and Bacon, S.: The Rossby radius in the Arctic Ocean, Ocean Science, 10, 967–975, https://doi.org/10.5194/os-10-967-2014, 2014.

Omand, M. M., D'Asaro, E. A., Lee, C. M., Perry, M. J., Briggs, N., Cetinić, I., and Mahadevan, A.: Eddy-driven subduction exports particulate organic carbon from the spring bloom, Science, 348, 222–225, https://doi.org/10.1126/science.1260062, 2015.

Oziel, L., Schourup-Kristensen, V., Wekerle, C., and Hauck, J.: The Pan-Arctic Continental Slope as an Intensifying Conveyer Belt for Nutrients in the Central Arctic Ocean (1985–2015), Global Biogeochemical Cycles, 36, e2021GB007 268, https://doi.org/10.1029/2021GB007268, 2022.

O'Brien, M. C., Melling, H., Pedersen, T. F., and Macdonald, R. W.: The role of eddies on particle flux in the Canada Basin of the Arctic Ocean, Deep Sea Research Part I: Oceanographic Research Papers, 71, 1–20, https://doi.org/10.1016/j.dsr.2012.10.004, 2013.

Pnyushkov, A., Polyakov, I. V., Padman, L., and Nguyen, A. T.: Structure and dynamics of mesoscale eddies over the Laptev Sea continental slope in the Arctic Ocean, Ocean Science, 14, 1329–1347, https://doi.org/10.5194/os-14-1329-2018, 2018.

Quintanilla-Zurita, A. and et al.: Intrahalocline eddy in the central Arctic from distributed observations during the MOSAiC winter, Ocean Science, (in prep.).

Rabe, B., Heuzé, C., Regnery, J., Aksenov, Y., Allerholt, J., Athanase, M., Bai, Y., Basque, C., Bauch, D., Baumann, T. M., Chen, D., Cole, S. T., Craw, L., Davies, A., Damm, E., Dethloff, K., Divine, D. V., Doglioni, F., Ebert, F., Fang, Y.-C., Fer, I., Fong, A. A., Gradinger, R., Granskog, M. A., Graupner, R., Haas, C., He, H., He, Y., Hoppmann, M., Janout, M., Kadko, D., Kanzow, T., Karam, S., Kawaguchi, Y., Koenig, Z., Kong, B., Krishfield, R. A., Krumpen, T., Kuhlmey, D., Kuznetsov, I., Lan, M., Laukert, G., Lei, R., Li, T., Torres-Valdés, S., Lin, L., Lin, L., Liu, H., Liu, N., Loose, B., Ma, X., McKay, R., Mallet, M., Mallett, R. D. C., Maslowski, W., Mertens, C., Mohrholz, V., Muilwijk, M., Nicolaus, M., O'Brien, J. K., Perovich, D., Ren, J., Rex, M., Ribeiro, N., Rinke, A., Schaffer, J., Schuffenhauer, I., Schulz, K., Shupe, M. D., Shaw, W., Sokolov, V., Sommerfeld, A., Spreen, G., Stanton, T., Stephens, M., Su, J., Sukhikh, N., Sundfjord, A., Thomisch, K., Tippenhauer, S., Toole, J. M., Vredenborg, M., Walter, M., Wang, H., Wang, L., Wang, Y., Wendisch, M., Zhao, J., Zhou, M., and Zhu, J.: Overview of the MOSAiC expedition: Physical oceanography, Elementa: Science of the Anthropocene, 10, https://doi.org/10.1525/elementa.2021.00062, 2022.

Rabe, B., Cox, C. J., Fang, Y.-C., Goessling, H., Granskog, Mats, A., Hoppmann, M., Hutchings, J. K., Kurmpen, T., Kuznetsov, I., Lei, R., Li, T., Maslowski, W., Nicolaus, M., Perovich, D., Persson, O., Regnery, J., Rigor, I., Shupe, M. D., Sokolov, V., Spreen, G., Stanton, T., Watkins, D. M., Blockley, E., Buenger, H. J., Cole, S., Fong, A., Haapala, J., Heuzé, C., Hoppe, C. J. M., Janout, M., Jutila, A., Katlein, C., Krishfield, R., Lin, L., Ludwig, V., Morgenstern, A., O'Brien, J., Quintanilla Zurita, A., Rackow, T., Riemann-Campe, K., Rohde, J., Shaw, W., Smolyanitsky, V., Solomon, A., Sperling, A., Tao, R., Toole, J., Tsamados, M., Zhu, J., and Zuo, G.: MOSAiC Distributed Network: observing the coupled Arctic system with multidisciplinary, coordinated platforms., submitted to Elementa: Science of the Anthropocene, 2023.

Regan, H., Lique, C., Talandier, C., and Meneghello, G.: Response of Total and Eddy Kinetic Energy to the Recent Spinup of the Beaufort Gyre, Journal of Physical Oceanography, 50, 575 – 594, https://doi.org/10.1175/JPO-D-19-0234.1, 2020.

Rubino, A., Androssov, A., and Dotsenko, S.: Intrinsic dynamics and long-term evolution of a convectively generated oceanic vortex in the Greenland Sea, Geophysical Research Letters, 34, https://doi.org/10.1029/2007GL030634, 2007.

Rudels, B.: Arctic Ocean Circulation, in: Encyclopedia of Ocean Sciences (Second Edition), edited by Steele, J. H., pp. 211–225, Academic Press, Oxford, second edition edn., https://doi.org/10.1016/B978-012374473-9.00601-9, 2009.

Ruggiero, G. A., Ourmières, Y., Cosme, E., Blum, J., Auroux, D., and Verron, J.: Data assimilation experiments using diffusive back-and-forth nudging for the NEMO ocean model, Nonlinear Processes in Geophysics, 22, 233–248, https://doi.org/10.5194/npg-22-233-2015, 2015.

Schulz, K., Mohrholz, V., Fer, I., Janout, M. A., Hoppmann, M., Schaffer, J., Koenig, Z., Rabe, B., Heuzé, C., Regnery, J., Allerholt, J., Fang, Y.-C., He, H., Kanzow, T., Karam, S., Kuznetsov, I., Kong, B., Liu, H., Muilwijk, M., Schuffenhauer, I., Sukhikh, N., Sundfjord, A., and Tippenhauer, S.: Turbulent microstructure profile (MSS) measurements from the MOSAiC drift, Arctic Ocean, https://doi.org/10.1594/PANGAEA.939816, 2022.

Scott, R. M., Pickart, R. S., Lin, P., Münchow, A., Li, M., Stockwell, D. A., and Brearley, J. A.: Three-Dimensional Structure of a Cold-Core Arctic Eddy Interacting with the Chukchi Slope Current, Journal of Geophysical Research: Oceans, 124, 8375–8391, https://doi.org/10.1029/2019JC015523, 2019.

Shepard, D.: A Two-Dimensional Interpolation Function for Irregularly-Spaced Data, in: Proceedings of the 1968 23rd ACM National Conference, ACM '68, p. 517–524, Association for Computing Machinery, New York, NY, USA, https://doi.org/10.1145/800186.810616, 1968.

Shupe, M., Rex, M., Dethloff, K., Damm, E., Fong, A. A., Gradinger, R., Heuzé, C., Loose, B., Makarov, A. S., Maslowski, W., Nicolaus, M., Perovich, D. K., Rabe, B., Rinke, A., Sokolov, V., and Sommerfeld, A.: Arctic Report Card 2020: The MOSAiC Expedition: A Year Drifting with the Arctic Sea Ice, Arctic Report Card, https://doi.org/10.25923/9g3v-xh92, 2020.

Sokolovskiy, M. A. and Verron, J.: Dynamics of Vortex Structures in a Stratified Rotating Fluid, Springer International Publishing, https://doi.org/https://doi.org/10.1007/978-3-319-00789-2, 2014.

Tippenhauer, S., Vredenborg, M., Heuzé, C., Ulfsbo, A., Rabe, B., Allerholt, J., Balmonte, J. P., Campbell, R. G., Castellani, G., Chamberlain, E., Creamean, J., D'Angelo, A., Dietrich, U., Droste, E., Eggers, L., Fang, Y.-C., Fong, A. A., Gardner, J., Graupner, R., Grosse, J., He, H., Hildebrandt, N., Hoppe, C. J. M., Hoppmann, M., Kanzow, T., Karam, S., Koenig, Z., Kong, B., Kuhlmey, D., Kuznetsov, I., Lan, M., Liu, H., Mallet, M., Mohrholz, V., Muilwijk, M., Müller, O., Olsen, L. M., Rember, R., Ren, J., Sakinan, S., Schaffer, J., Schmidt, K., Schuffenhauer, I., Schulz, K., Shoemaker, K., Spahic, S., Sukhikh, N., Svenson, A., Torres-Valdés, S., Torstensson, A., Wischnewski, L., and Zhuang, Y.: Physical oceanography based on ship CTD during POLARSTERN cruise PS122., https://doi.org/10.1594/PANGAEA.959963, 2023a.

Tippenhauer, S., Vredenborg, M., Heuzé, C., Ulfsbo, A., Rabe, B., Allerholt, J., Balmonte, J. P., Campbell, R. G., Castellani, G., Chamberlain, E., Creamean, J., D'Angelo, A., Dietrich, U., Droste, E., Eggers, L., Fang, Y.-C., Fong, A. A., Gardner, J., Graupner, R., Grosse, J., He, H., Hildebrandt, N., Hoppe, C. J. M., Hoppmann, M., Kanzow, T., Karam, S., Koenig, Z., Kong, B., Kuhlmey, D., Kuznetsov, I., Lan, M., Liu, H., Mallet, M., Mohrholz, V., Muilwijk, M., Müller, O., Olsen, L. M., Rember, R., Ren, J., Sakinan, S., Schaffer, J., Schmidt, K., Schuffenhauer, I., Schulz, K., Shoemaker, K., Spahic, S., Sukhikh, N., Svenson, A., Torres-Valdés, S., Torstensson, A., Wischnewski, L., and Zhuang, Y.: Physical oceanography based on Ocean City CTD during POLARSTERN cruise PS122., https://doi.org/10.1594/PANGAEA.959964, 2023b.

Toole, J. M. and Krishfield, R. A.: Oceanographic Institution Ice-Tethered Profiler Program (2016). Ice-Tethered Profiler observations: Vertical profiles of temperature, salinity, oxygen, and ocean velocity from an Ice-Tethered Profiler buoy system. [indicate subset used]. NOAA National Centers for Environmental Information. Dataset., Tech. rep., https://doi.org/10.7289/v5mw2f7x, accessed 13.7.2021, 2016.

Troupin, C., Barth, A., Sirjacobs, D., Ouberdous, M., Brankart, J.-M., Brasseur, P., Rixen, M., Alvera-Azcárate, A., Belounis, M., Capet, A., Lenartz, F., Toussaint, M.-E., and Beckers, J.-M.: Generation of analysis and consistent error fields using the Data Interpolating Variational Analysis (DIVA), Ocean Modelling, 52-53, 90–101, https://doi.org/10.1016/j.ocemod.2012.05.002, 2012.

von Appen, W.-J., Baumann, T. M., Janout, M., Koldunov, N., Lenn, Y.-D., Pickart, R. S., Scott, R. B., and Wang, Q.: Eddies and the Distribution of Eddy Kinetic Energy in the Arctic Ocean, Oceanography, 35, pp. 42–51, https://www.jstor.org/stable/27182695, 2022.

Wang, Q., Koldunov, N. V., Danilov, S., Sidorenko, D., Wekerle, C., Scholz, P., Bashmachnikov, I. L., and Jung, T.: Eddy Kinetic Energy in the Arctic Ocean From a Global Simulation With a 1-km Arctic, Geophysical Research Letters, 47, e2020GL088 550, https://doi.org/10.1029/2020GL088550, 2020.

Watanabe, E.: Beaufort shelf break eddies and shelf-basin exchange of Pacific summer water in the western Arctic Ocean detected by satellite and modeling analyses, Journal of Geophysical Research: Oceans, 116, https://doi.org/10.1029/2010JC006259, 2011.

Zhao, M., Timmermans, M.-L., Cole, S., Krishfield, R., Proshutinsky, A., and Toole, J.: Characterizing the eddy field in the Arctic Ocean halocline, Journal of Geophysical Research: Oceans, 119, 8800–8817, https://doi.org/10.1002/2014JC010488, 2014.

Zhao, M., Timmermans, M.-L., Cole, S., Krishfield, R., and Toole, J.: Evolution of the eddy field in the Arctic Ocean's Canada Basin, 2005-2015, Geophysical Research Letters, 43, 8106–8114, https://doi.org/10.1002/2016GL069671, 2016.